# X-Ray Photoabsorption of Density-sensitive Metastable States in Ne VII, Fe XXII, and Fe XXIII

René Steinbrügge[1] , Steffen Kühn[2] , Fabrizio Nicastro[3] , Ming Feng Gu[4] , Moto Togawa[2] , Moritz Hoesch[1] ,
Jörn Seltmann[1], Ilya Sergeev[1], Florian Trinter[5,6] , Sonja Bernitt[2,7,8,9] , Chintan Shah[2,10,11] , Maurice A. Leutenegger[10] , and
José R. Crespo López-Urrutia[2]

[1] Deutsches Elektronen-Synchrotron DESY, Notkestr. 85, D-22607 Hamburg, Germany; rene.steinbruegge@med.uni-heidelberg.de
[2] Max-Planck-Institut für Kernphysik, Saupfercheckweg 1, D-69117 Heidelberg, Germany
[3] Instituto Nazionale di Astrofisica (INAF), Osservatorio Astronomico di Roma, Rome, Italy
[4] Space Science Laboratory, University of California, Berkeley, CA 94720, USA
[5] Institut für Kernphysik, Goethe-Universität Frankfurt am Main, Max-von-Laue-Straße 1, D-60438 Frankfurt am Main, Germany
[6] Molecular Physics, Fritz-Haber-Institut der Max-Planck-Gesellschaft, Faradayweg 4-6, D-14195 Berlin, Germany
[7] Helmholtz-Institut Jena, Fröbelstieg 3, D-07743 Jena, Germany
[8] GSI Helmholtzzentrum für Schwerionenforschung, Planckstraße 1, D-64291 Darmstadt, Germany
[9] Institut für Optik und Quantenelektronik, Friedrich-Schiller-Universität Jena, Max-Wien-Platz 1, D-07743 Jena, Germany
[10] NASA Goddard Space Flight Center, 8800 Greenbelt Rd., Greenbelt, MD 20771, USA
[11] Southeastern Universities Research Association, 1201 New York Ave. NW, Washington, DC 20005, USA
Received 2022 March 19; revised 2022 September 30; accepted 2022 October 13; published 2022 December 22

## Abstract

Metastable states of ions can be sufficiently populated in absorbing and emitting astrophysical media, enabling spectroscopic plasma-density diagnostics. Long-lived states appear in many isoelectronic sequences with an even number of electrons, and can be fed at large rates by various photonic and electronic mechanisms. Here, we experimentally investigate beryllium-like and carbon-like ions of neon and iron that have been predicted to exhibit detectable features in astrophysical soft X-ray absorption spectra. An ion population generated and excited by electron impact is subjected to highly monochromatic X-rays from a synchrotron beamline, allowing us to identify K$\alpha$ transitions from metastable states. We compare their energies and natural line widths with state-of-the-art theory and benchmark level population calculations at electron densities of $10^{10.5}$ cm$^{-3}$.

*Unified Astronomy Thesaurus concepts:* Atomic physics (2063); Plasma astrophysics (1261); Spectroscopy (1558); Laboratory astrophysics (2004); Ionization (2068); Line positions (2085); Line intensities (2084); Atomic data benchmarking (2064)

## 1. Introduction

Neon and iron are among the most abundant elements in the universe (Asplund et al. 2009) and appear in all possible ionization stages. Thus, accurate knowledge of emission and absorption spectra of their ions in charge states from neutral to bare is crucial for the analysis of space-based X-ray observations aiming to determine elemental abundances, temperatures, densities, and velocity fields of the objects observed. First experiments on Be-like Ne VII were reported by Bockasten et al. (1963), who analyzed the ultraviolet (UV) and vacuum-ultraviolet (VUV) spectra of highly ionized light elements in high-temperature plasmas produced in a toroidal discharge apparatus. In the following decades, magnetically confined fusion plasmas, beam-foil spectroscopy, and electron beam ion traps (EBITs) have delivered more experimental data on this ion, extending the observed range to cover the visible up to the X-ray region. A comprehensive review on Ne VII can be found in Kramida & Buchet-Poulizac (2006). Both Ne and Fe (appearing as Be-like Fe XXIII in hotter plasmas) are quintessential for astrophysical diagnostics of ionized gas, such as highly ionized, high-velocity outflows from active galactic nuclei (AGN) or X-ray binaries. These winds are crucial for feeding back energy and chemically enriched material into their

surroundings throughout the evolution of the universe. Other Ne and Fe populations are found in hot, diffuse plasmas, in the warm–hot intergalactic medium (Cen & Ostriker 2006), galactic hot halos, the circumgalactic medium, and the radiative cores of stars.

Ubiquitous, ionized outflowing winds in AGN (McKernan et al. 2007; Tombesi et al. 2013) are thought to be critical components of galactic feedback. As most of the outflowing column density in AGN is only detected in X-rays (e.g., Kaastra et al. 2000; Kaspi et al. 2000), it is crucial to understand the X-ray phases of the outflow (Laha et al. 2021, and references therein) in order to quantify their feedback effects. Analogous outflows are also seen in X-ray binaries (Paerels et al. 2000; Miller et al. 2008). The physical properties of these outflows (mass, momentum, and energy outflow rates) are still extremely uncertain. This is mainly because most of the direct observables only provide estimates of the gas kinematics, ionization state, and column density that are not independent of the gas hydrogen-equivalent volume density $n_H$ and distance $D$ from the ionizing sources. Both parameters are vital to derive the mass and thus the momentum and energy outflow rates of the winds.

Indeed, one can observationally estimate the ionization state of the gas, typically parameterized at equilibrium through the ionization parameter $U$. This is defined as the ratio between the volume density of ionizing photons at the illuminated surface of the cloud (i.e., $n_{ph} = Q/(4\pi D^2 c)$, where $Q$ is the rate of ionizing photons and $D$ the distance of the ionizing source from

the gas) and the electron density in the gas: $U = n_{ph}/n_e$. Thus, from an estimate of $U$ one can infer an estimate of the products $D^2 n_H$ ($n_H \approx 1.2 n_e$ for a fully ionized gas), but not independently $D$ or $n_H$. Without independent estimates of these two parameters, an estimate of the mass load of the outflow is impossible.

The distance $D$ is too small to be spatially resolved even in the closest in AGNs, so volume density estimates are needed. One possibility, in gas undergoing photoionization by variable sources, is to follow the evolution of the gas ionization stage with time. Equilibration time, indeed, depends critically on the volume density of the gas; thus time-resolved spectroscopy of AGN absorbers performed with proper time-evolving photoionization models, could provide estimates of the gas density (e.g., Krolik & Kriss 1995; Nicastro et al. 1999).

Another very efficient way of determining $n_H$ is the analysis of absorption lines from density-sensitive metastable levels. Recently, Mao et al. (2017) proposed to employ X-ray and UV absorption lines from metastable levels in Be-like, B-like, and C-like ions as density diagnostics for both mildly ionized (i.e., "warm absorbers"; e.g., Nandra & Pounds 1992) and highly ionized high-velocity (i.e., ultrafast outflows—UFO; e.g., Tombesi et al. 2013) outflows in AGNs. They predict that in a purely photoionized plasma several metastable states of Be-like and C-like ions of astrophysically abundant elements (e.g., C, N, and O, for "warm absorbers" and Fe for UFOs) can be sufficiently populated over a broad density range.

Such observations could certainly become possible in the near future, thanks to the advent of high-throughput, moderate-spectral-resolution X-ray spectroscopic missions like the X-Ray Imaging and Spectroscopy Mission (XRISM; Tashiro et al. 2018; XRISM Science Team 2020) and the Advanced Telescope for High-Energy Astrophysics (ATHENA; Barret et al. 2016, 2020) with spectral resolutions of 5 eV and 2.5 eV, respectively. Unfortunately, however, little is known on the exact energies, widths, and cross sections of these inner-shell metastable transitions, and both theoretical calculations and laboratory experiments are therefore needed to bridge the gap before these missions begin operating.

So far, laboratory measurements of photoabsorption from metastable states in ions have only been performed for low-Z elements (e.g., B, C, N, and O for Be-like (Muller et al. 2005; Scully et al. 2013; Al Shorman et al. 2014; McLaughlin et al. 2016) as well as O for C-like systems (Bizau et al. 2015)) using the ion–photon merged-beam technique.

Here, we report on first absorption measurements of X-ray transitions in Ne VII, Fe XXIII, and Fe XXI from metastable initial states in a hot, optically thin plasma produced and confined in an EBIT (Levine et al. 1988, 1989), and compare them with advanced theoretical predictions.

## 2. Experiment

We used the well-established combination of an EBIT and a synchrotron radiation source to study the transitions of interest (Simon et al. 2010a, 2010b; Rudolph et al. 2013; Steinbrügge et al. 2015; Kühn et al. 2020; Leutenegger et al. 2020). A schematic overview of the setup is shown in Figure 1. For this experiment, we used PolarX-EBIT, a portable version of the Heidelberg compact EBITs (Micke et al. 2018). It features an off-axis electron gun, which leaves the main axis of the experiment obstacle-free. The electron beam is compressed by a magnetic field produced by an arrangement of permanent magnets, reaching 0.86 T at the trap center. The elements of interest are injected into the trap region in the form of very tenuous atomic or molecular beams. When molecules cross the electron beam, they dissociate, delivering atoms of the chosen element, which are subsequently ionized by successive electron impacts. The resulting, positively charged ions stay in narrow orbits within or around the electron beam, forming a cylindrical ion cloud axially confined by voltages applied to the trap electrodes. The charge-state distribution of the plasma depends on a few operating parameters and is adjusted to maximize the ion species of interest.

In order to study the interaction with photons, a beam of monochromatic X-rays propagates through the ion cloud, with its photon energy being scanned across a range containing the resonant transitions. Following excitation, the relaxation through X-ray photon emission of the populated electronic states is recorded using a silicon-drift detector (SDD) with a resolution of approximately 100–125 eV FWHM in the range of interest. To obtain the spectrum, all photons registered in a region of interest around the expected energy are summed up. Despite the electron-beam energy being lower than the X-ray energy, it can still generate a low X-ray background in this energy range by radiative recombination into excited states, or pileup in the detector.

As the K-shell resonance energies of neon and iron differ by nearly 1 order of magnitude, the reported measurements were performed in two separate campaigns at the PETRA III synchrotron radiation source using two different beamlines, P04 for soft X-rays Viefhaus et al. (2013) and P01 for hard X-rays Wille et al. (2010), respectively.

At the soft X-ray beamline P04, circularly polarized photons were produced by an APPLE-II undulator (Bahrdt et al. 2008). They passed through the monochromator, which is equipped with a grating having a variable line spacing of $\approx 1200$ lines mm$^{-1}$, reaching a resolving power of $E/\Delta E_{FWHM} = 14{,}000$ at 895 eV. Downstream of PolarX-EBIT, a gas cell furnished with several microchannel plates mounted on its side was used to detect photoions produced by the photon beam passing through a neon gas target, analogously to Leutenegger et al. (2020). The photon energy was calibrated using the well-known transitions K$\alpha$, K$\beta$, and K$\gamma$ in He-like neon measured in the EBIT, as well as near K-shell photoionization resonances of Ne I in the gas cell. Reference energies for the calibration were taken from Yerokhin & Surzhykov (2019) and Muller et al. (2017), respectively. The former reference states uncertainties for the K$\alpha$, K$\beta$, and K$\gamma$ transitions below 1 meV. However, due to an inadequate interpolation correction of the angular encoder of the P04 monochromator, the calibration accuracy is limited to 30 meV. Repeatedly scanning the same transitions over hours ensured that slow energy drifts of the monochromator were identified and corrected.

The measurements of Be-like and C-like iron were performed at beamline P01. Two 5 m undulators produced an intense, horizontally polarized X-ray beam. It then passed a high-heat-load dual-crystal monochromator (DCM) using the $\langle 311 \rangle$ reflection of silicon, yielding a resolution of 200 meV at 6.5 keV photon energy. The outgoing beam was focused by a stack of beryllium lenses down to a spot size of approximately $270 \times 240 \,\mu$m in the ion-trap center. To measure the transitions, the energy-resolved fluorescence signal from the SDD was recorded while the photon energy was scanned by stepwise varying the DCM Bragg angle.
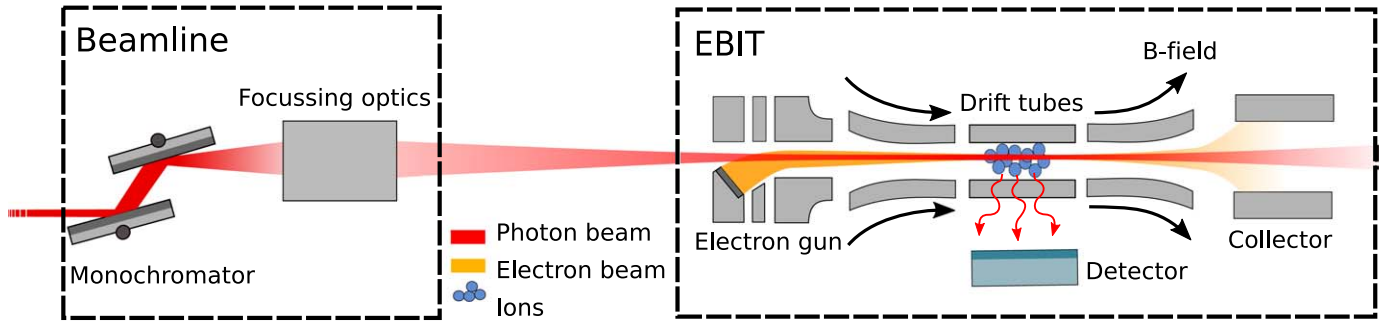
**Figure 1.** Scheme of the experiment at PETRA III. The photon beam coming from the undulator passes the monochromator and is focused onto the coaxially aligned, elongated ion cloud confined inside the electron beam ion trap. Fluorescence photons emitted by the trapped ions are registered by a silicon-drift detector mounted perpendicular to the beam.
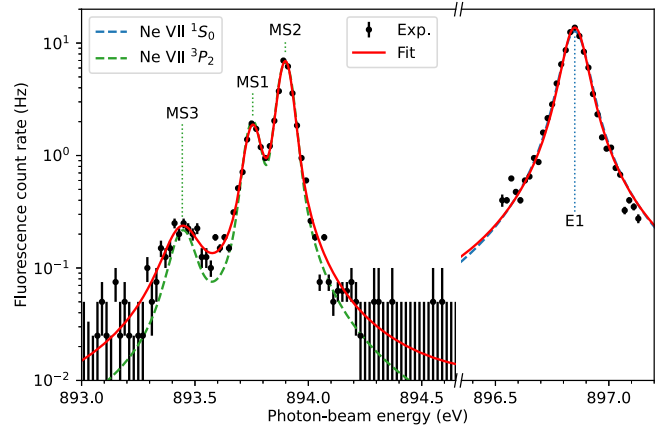
## 3. Results

### 3.1. Be-like Ne VII

For the Ne VII measurements, the electron-beam energy was set to 360 eV and the current to ≈0.9 mA. These relatively low operational settings and a high gas-injection pressure ensured that the charge-state distribution of the plasma stretched from He-like down to Be-like, as needed. Furthermore, the low beam current combined with a shallow axial trap of 20 V favored an increased evaporative cooling from the trap (Penetrante et al. 1991) that reduced the Doppler broadening of the observed transitions (Beiersdorfer et al. 1996).

The signal measured across the energy range of the Be-like neon transitions is depicted in Figure 2. To model the data, a Voigt profile was fitted to each peak. The respective Gaussian width of each peak is caused by the limited resolution of the monochromator and Doppler broadening due to the high ion temperature in the trap. Both effects are nearly the same for all transitions ($46 \pm 5$ meV), while each line has its own Lorentzian width from the finite lifetime of the excited levels. The strongest resonance at 896.850 eV, also known as E1, arises from the transition from the ground state of the Be-like ion $1s^2 2s^2\,{}^1S_0$ to the excited state $1s2s^2 2p\,{}^1P_1$. This upper state has several decay channels, dominated by nonradiative, and thus here undetected, Auger–Meitner processes. Hence, the natural Lorentzian width is rather large, whereas the fluorescence signal is weak, due to its small radiative branching ratio, predicted by calculations to be only 5.8%.

Three transitions at 893.755 eV, 893.899 eV, and 893.444 eV, marked as MS1, MS2, and MS3, were identified as originating from the metastable initial state $1s^2 2s 2p\,{}^3P_2$ being excited to the states $1s2s2p^2\,{}^3P_1$, $1s2s2p^2\,{}^3P_2$, and $1s2s2p^2\,{}^3D_3$, respectively. In contrast to E1, the calculated branching ratios for the upper states of MS1 and MS2 are predominantly radiative. Thus, their observed intensities are rather strong, although in the EBIT the metastable initial state is much less populated than the ground state. The spectral resolution of ATHENA will be sufficient to separate these metastable and ground-state transitions. Although MS1, MS2, and MS3 will not be resolved from each other, as they originate from the same metastable state, they will allow estimates on the population balance.

### 3.2. Be-like Fe XXIII

To produce Be-like Fe XXIII, PolarX-EBIT was operated with an electron-beam energy of 3000 eV and a current of 16.4 mA. The photon-beam energy was scanned eight times



**Figure 2.** Results for Be-like Ne VII: fluorescence count rate vs. incoming photon energy. Error bars display the $1\sigma$ statistical uncertainties. The red curve shows a fit of four Voigt profiles to the line E1 and three other transitions from metastable states. The blue and green dashed curves show the contributions of the $^1S_0$ ground state and the $^3P_2$ metastable state from our population model.
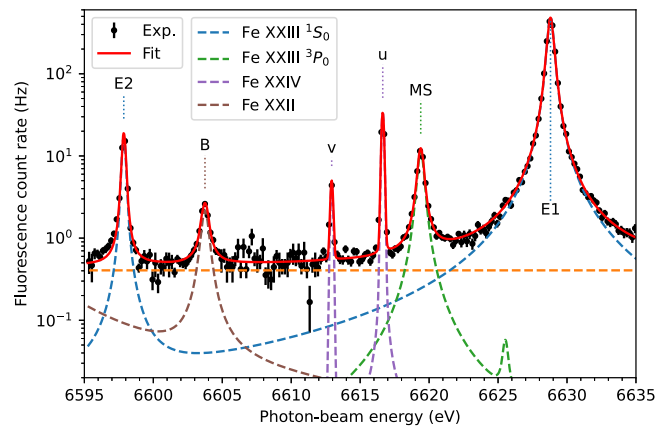


**Figure 3.** Results for Be-like Fe XXIII: fluorescence count rate vs. incoming photon energy. The shown data are binned to 0.2 eV intervals for clarity. Red curve: fit of six Voigt profiles to ground-state transitions in Li-like (u, v), Be-like (E1, E2), and B-like (B) Fe ions. MS originates from the excitation of a metastable state in Be-like Fe XXIII. Dashed curves: contributions of the different initial states derived from our population model. Dashed orange line: fit of experimental background.

between 6595 and 6635 eV. Due to the large differences in line intensity, we varied the measurement time for each step between 3 s and 10 s to ensure sufficient statistics, resulting in a total measurement time of 6.5 hr.

**Table 1**
Measured and Calculated Line Energies and Widths

| Element | Line | Initial | Excited | $E_{exp}$ (eV) | $E_{Lit}$ | $E_{FAC}$ (eV) | $\Gamma_{exp}$ (meV) | $\Gamma_{FAC}$ (meV) |
|---|---|---|---|---|---|---|---|---|
| Ne VII | E1 | $1s^22s^2\ {}^1S_0$ | $1s2s^22p\ {}^1P_1$ | 896.850(1)(30) | 897.13[a] | 896.877 | 84(4) | 85.3 |
| Ne VII | MS1 | $1s^22s2p\ {}^3P_2$ | $1s2s2p^2\ {}^3P_1$ | 893.755(2)(30) | | 893.751 | 47(7) | 27.2 |
| Ne VII | MS2 | $1s^22s2p\ {}^3P_2$ | $1s2s2p^2\ {}^3P_2$ | 893.899(1)(30) | 893.32[a] | 893.889 | 34(3) | 25.2 |
| Ne VII | MS3 | $1s^22s2p\ {}^3P_2$ | $1s2s2p^2\ {}^3D_3$ | 893.444(15)(30) | 893.3(2)[b] | 893.422 | 159(41) | 87.4 |
| Fe XXIII | E2 | $1s^22s^2\ {}^1S_0$ | $1s2s^22p\ {}^3P_1$ | 6597.858*(3)(68) | 6596.0 | 6597.946 | $168(^{+16}_{-27})$ | 174 |
| Fe XXII | B | $1s^22s^22p\ {}^2P_{1/2}$ | $1s2s^22p^2\ {}^2P_{3/2}$ | 6603.747(15)(68) | 6601.2 | 6604.039 | $502(^{+61}_{-64})$ | 521 |
| Fe XXIV | v | $1s^22s\ {}^2S_{1/2}$ | $1s2s2p\ {}^4P_{1/2}$ | 6612.936(5)(68) | 6613.5 | 6613.056 | < 42 | 3 |
| Fe XXIV | u | $1s^22s\ {}^2S_{1/2}$ | $1s2s2p\ {}^4P_{3/2}$ | 6616.638(1)(68) | 6616.7 | 6616.760 | < 20 | 11 |
| Fe XXIII | MS | $1s^22s2p\ {}^3P_0$ | $1s2s2p^2\ {}^3P_1$ | 6619.392(5)(68) | 6619.6 | 6619.588 | $394(^{+19}_{-28})$ | 409 |
| Fe XXIII | E1 | $1s^22s^2\ {}^1S_0$ | $1s2s^22p\ {}^1P_1$ | 6628.804*(1)(68) | 6628.8 | 6628.866 | $396(^{+7}_{-14})$ | 391 |
| Fe XX | N | $1s^22s^22p^3\ {}^4S_{3/2}$ | $1s2s^22p^4\ {}^2P_{3/2}$ | $6535.186(^{+43}_{-35})(68)$ | 6534.4 | 6535.693 | $810(^{+150}_{-101})$ | 812 |
| Fe XXI | MS1 | $1s^22s^22p^2\ {}^3P_1$ | $1s2s^22p^3\ {}^3D_2$ | $6536.924(^{+113}_{-211})(68)$ | 6535.8 | 6537.228 | $435(^{+620}_{-181})$ | 467 |
| Fe XXI | C1 | $1s^22s^22p^2\ {}^3P_0$ | $1s2s^22p^3\ {}^3D_1$ | 6544.225*(1)(68) | 6543.7 | 6544.411 | 496(4) | 517 |
| Fe XXI | MS2 | $1s^22s^22p^2\ {}^3P_1$ | $1s2s^22p^3\ {}^3S_1$ | $6547.727(^{+144}_{-121})(68)$ | 6545.8 | 6547.905 | 583(11) | 621 |
| Fe XXI | MS3 | $1s^22s^22p^2\ {}^3P_2$ | $1s2s^22p^3\ {}^1D_2$ | 6548.417(44)(68) | 6547.5 | 6548.635 | $413(^{+122}_{-107})$ | 547 |
| Fe XXI | MS4 | $1s^22s^22p^2\ {}^3P_2$ | $1s2s^22p^3\ {}^3P_1$ | 6550.434(47)(68) | 6551.3 | 6550.630 | $205(^{+109}_{-91})$ | 526 |
| Fe XXII | B | $1s^22s^22p\ {}^2P_{1/2}$ | $1s2s^22p^2\ {}^4P_{1/2}$ | 6553.070(10)(68) | 6553.8 | 6553.422 | 115(24) | 211 |
| Fe XXI | C2 | $1s^22s^22p^2\ {}^3P_0$ | $1s2s^22p^3\ {}^3S_1$ | 6556.879*(4)(68) | 6555.2 | 6557.093 | 583(11) | 622 |

**Note.** Listed are the initial and excited states, the transition energy $E$, and the natural line width $\Gamma$, both from our experiment and our FAC calculations. Uncertainties are given on a $1\sigma$ level. For $E_{exp}$ the second parenthesis states the systematic uncertainty of the photon-beam energy calibration. Transition energies marked with * are fixed to values from Rudolph et al. (2013) by the energy calibration. Literature values $E_{Lit}$ are taken from Mao et al. (2017; a), Wargelin et al. (2001; b), and Palmeri et al. (2003; Fe data).

The result, displayed in Figure 3, is showing six lines. They could be identified as absorption in Li-like, Be-like, and B-like iron ions, one of them being an excitation from the metastable $1s^22s2p\ {}^3P_0$ state in Fe XXIII. It is well separated from the Fe XXIII ground-state transitions, so that it could be resolved with XRISM and ATHENA, if the Li-like population is sufficiently weak to avoid a blend with line u.

The photon-beam energy scale was calibrated by a linear interpolation, which fixed the transition energies of the E1 and E2 transitions to the values measured by Rudolph et al. (2013). The uncertainties of those values result in a systematic uncertainty for this measurement. The transition energies and line widths listed in Table 1 were calculated using a maximum-likelihood fit of Voigt profiles with a common Gaussian width. When each charge state was fitted individually, their Gaussian widths varied between 180 and 230 meV. As the Gaussian and Lorentzian widths are correlated in the fit, two additional fits were performed with a shared Gaussian width fixed at the maximum and minimum value, giving an estimate for the associated extra uncertainty for the natural line widths. The X-ray background produced by the electron beam was included in the fit as a constant offset.

As the Li-like transitions u and v both have low Auger–Meitner decay rates, their natural line widths are much smaller than the experimental Gaussian width; thus we could only estimate an upper limit for them.

By comparing the line intensities to calculations, we determined a relative population of the $^3P_0$ metastable state in Be-like Fe XXIII of 2.6% ± 0.1% of the $^1S_0$ ground state.

### 3.3. C-like Fe XXI

For the measurements in C-like Fe XXI, the electron-beam energy and current were reduced to 2000 eV and 15.9 mA, respectively. The photon-beam energy was scanned seven times between 6530 and 6565 eV for a total measurement time of 7.5 hr.

The results are shown in Figure 4. In addition to the strong lines C1 and C2 originating from the C-like $^3P_0$ ground state, we identified four transitions from the metastable $^3P_1$ and $^3P_2$ initial states, as well as some from the B-like and N-like ground states. To calibrate the photon energy, we used the values for the C1 and C2 transition measured by Rudolph et al. (2013). The fits yielded a common Gaussian width of 233 ± 9 meV. We list the measured transition energies and line widths in Table 1.

In the present case, the observed lines excited from metastable initial states are weak and superimposed on the wings of the C1 transition, such that the energy measurement accuracy is worse than for those of Be-like ions. However, their statistical uncertainty is similar to the systematic uncertainty of the photon-energy calibration.

By comparison with calculated line intensities, we estimate a population of the metastable states of 0.26% ± 0.06% for the $^3P_1$ and 0.63% ± 0.11% for the $^3P_2$ state.

While lines MS2 and MS3 will be blended when observed with ATHENA or XRISM, MS1 and MS4 could be resolved and will allow estimations of the $^3P_1$ and $^3P_2$ population balance.

### 3.4. Calculations

We used the Flexible Atomic Code (FAC) developed by Gu (2008) to calculate the transition energies and radiative as well as autoionizing transition rates. To account for electron-correlation effects more accurately, we combined configuration interaction (CI) and second-order many-body perturbation theory (MBPT) to obtain the level energies and radiative transition rates, while Auger–Meitner decay rates were obtained in the standard CI approximation (Gu et al. 2006).
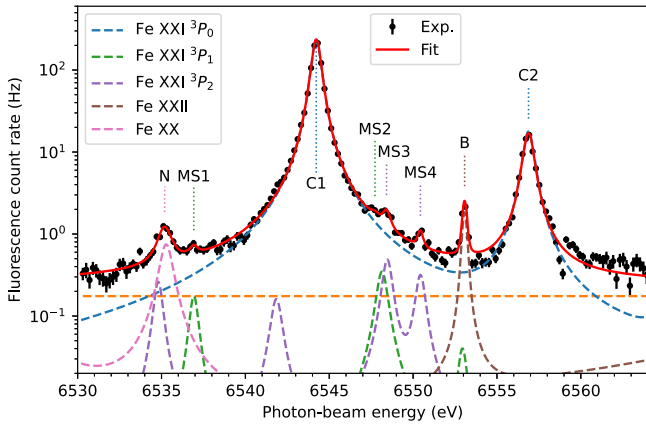
**Figure 4.** Result for C-like Fe XXI: Fluorescence count rate vs. incoming photon energy. Red curve: fit of eight Voigt profiles to ground-state transitions in B-like (B), C-like (C1, C2), and N-like (N) Fe ions. MS1 to MS4 originate from metastable initial states in C-like Fe XXI. Dashed curves: contributions of the different initial states derived from our population model. Dashed orange line: fit of experimental background.

In the present calculation, the reference space included configurations of $1s^2 2l^q$ and $1s2l^{q+1}$ with $q = 2$ for Be-like ions and $q = 4$ for C-like ions. Correlation effects within the reference space were accounted to all orders with the CI approximation. Correlation effects with the orthogonal space defined by all single and double excitations from the reference space were treated in second-order MBPT by diagonalizing the effective Hamiltonian matrix within the reference space. The matrix elements of the effective Hamiltonian contained second-order MBPT corrections. The radial basis functions used to construct the reference and orthogonal spaces were derived from the solutions to the Dirac equation of a model potential, which was optimized on the $1s^2 2l^q$ or $1s2l^{q+1}$ configurations for the respective levels. The wave functions were contained in a spherical box with radius determined such that all $n \leqslant 2$ orbitals had negligible amplitudes outside the box. Such a boundary condition discretized the continuum so that correlation effects could be included without complications of integrating over the orbitals in the continuum spectrum. Frequency-dependent Breit interaction was included in both CI expansion and MBPT corrections. Lamb shifts due to vacuum polarization and self-energy corrections were computed using the model QED operator of Shabaev et al. (2015). By adding up the rates of all radiative and Auger–Meitner decay channels of an excited state, we obtained the natural line width of the state. The results are listed in Table 1.

Figure 5(a) compares the calculated and experimental energies. They agree within error bars for the neon measurement, while for the Be-like and C-like iron there is an overall shift of approximately 0.1 eV and 0.2 eV, respectively. This difference could be due to offsets in the calculated energy levels or an incorrect energy calibration in the experiment. However, the latter would not explain the relative deviation of the boron-like and nitrogen-like transitions.

Taking their uncertainties into account, we find that the experimental natural line widths for most lines agree within 10% with the calculated values, as shown in Figure 5(b). The mean relative deviation $\Delta = \sqrt{\sigma_{\exp}^2 + (\Gamma_{\exp} - \Gamma_{FAC})^2}$ for each ion was used to assign a confidence interval to the calculated line strengths used in the population estimation.
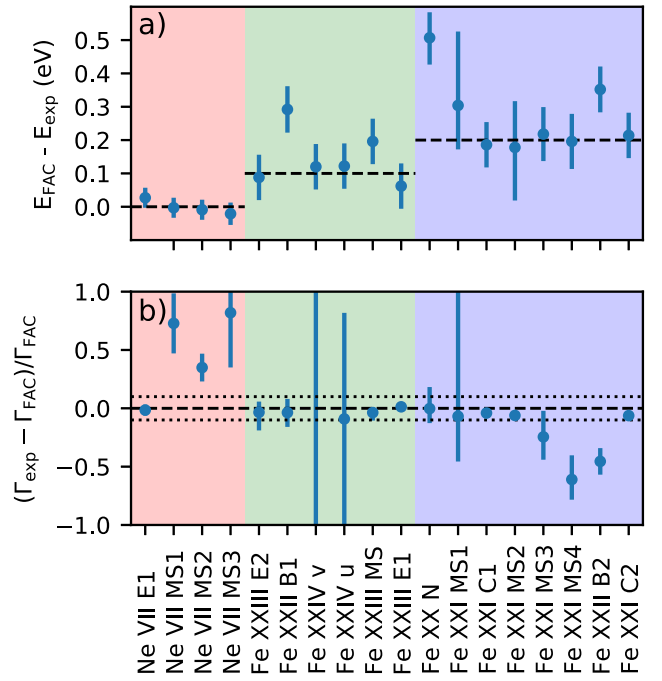


**Figure 5.** Comparison of theory and experiment. (a) Difference between calculated and measured transition energies. Background colors indicate different measurement setups and thus different experimental energy calibrations. The dashed lines indicate offsets of 0 eV, 0.1 eV, and 0.2 eV, respectively. (b) Relative deviation of calculated and measured natural line widths. The dotted lines indicate a ±10% deviation.

### 3.5. State-population Balance

To estimate the state-population balance, we used the results of our FAC calculations to build a model spectrum for each initial state. Every line was represented by a Voigt profile, where the center and Lorentzian width were the calculated transition energy and line width, respectively. The area of the profile was set to the line strength multiplied by a factor to account for polarization effects (see Appendix A). A weighted sum of these spectra was fitted to the measured data, with the weights and a shared Gaussian width as free parameters. To account for uncertainties in calculated data and experimental energy calibration, the line centers were allowed to vary by ±1 eV. The results of these model fits are also shown in Figures 2, 3, and 4. The ratio of the fitted weights gives the population ratio present in the ion cloud. These results are listed in Table 2.

We calculated the theoretical state-population balance as a function of the density and charge-state distribution using the FAC collisional radiative model (CRM). For these calculations we used a simplified CI-only atomic model. We then compared our calculations with the measured state-population balances. The results are shown in Figures 6 and 7, as well as Figures 8–12 in Appendix B.

In particular, we found that the populations of the $^3P_2$ and $^3P_1$ states of C-like Fe (Figure 6) are good density diagnostics in the density regime of our experiment, and that these state populations only weakly depend on charge balance. The inferred effective density of $\log n_e / \text{cm}^3 = 10.55$ is a factor of 18 lower than the estimated electron density in the beam of $\log n_e / \text{cm}^3 = 11.8$ (Micke et al. 2018). Such a result is expected, as the trapped ions in thermal motion only spend a fraction of their time traversing the electron beam. The
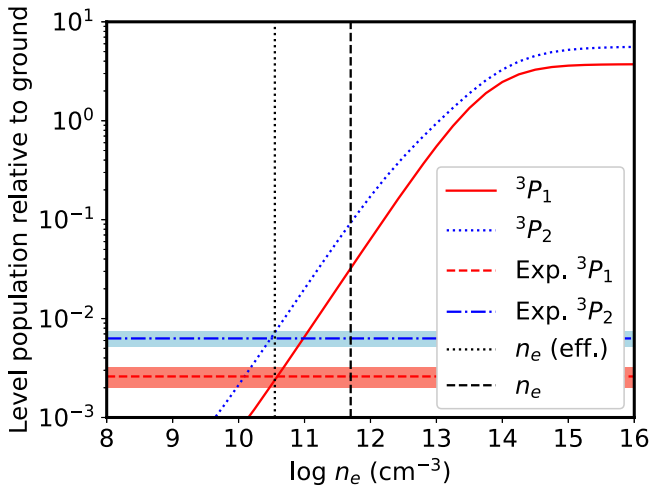
**Figure 6.** Density dependence of theoretical level populations for the two most important metastable states of C-like Fe, compared with measured populations. The geometric electron density of the beam is estimated to be $\log n_e = 11.8$ (vertical black dashed line). The measurements are consistent with an effective density of $\log n_e = 10.55$, which is lower by a factor of 18 (vertical black dotted line). This reflects the fact that the trapped ion cloud has a larger radius than the electron beam, and thus trapped ions only spend a fraction of their time crossing the electron beam. The ion gyroradius corresponding to this density is 150 $\mu$m, nearly 4 times larger than the electron-beam radius.

**Table 2**
Estimation of the Population Balance

| Ion | State | | R(%) | ΔR(%) |
|---|---|---|---|---|
| Ne VII | $1s^2 2s^2$ | $^1S_0$ | 100.0 | (1.9) |
| Ne VII | $1s^2 2s2p$ | $^3P_2$ | 11.9 | (0.30)(3.2) |
| Fe XXIII | $1s^2 2s^2$ | $^1S_0$ | 100.0 | (0.48) |
| Fe XXIII | $1s^2 2s2p$ | $^3P_0$ | 2.58 | (0.04)(0.12) |
| Fe XXIV | $1s^2 2s$ | $^2S_{1/2}$ | 75.6 | (1.1)(N/A) |
| Fe XXII | $1s^2 2s^2 2p$ | $^2P_{1/2}$ | 85.7 | (3.4)(22.6) |
| Fe XXI | $1s^2 2s^2 2p^2$ | $^3P_0$ | 100.00 | (0.38) |
| Fe XXI | $1s^2 2s^2 2p^2$ | $^3P_1$ | 0.26 | (0.06)(0.01) |
| Fe XXI | $1s^2 2s^2 2p^2$ | $^3P_2$ | 0.63 | (0.11)(0.03) |
| Fe XXII | $1s^2 2s^2 2p$ | $^2P_{1/2}$ | 57.1 | (3.3)(15.1) |
| Fe XX | $1s^2 2s^2 2p^3$ | $^4S_{3/2}$ | 114.6 | (8.8)(18.0) |

**Note.** Given are the population ratios compared to the Be-like or C-like ground state, which thus have a ratio of 100%. The first bracket states the statistical uncertainty of the fit. The second one is derived from assigned confidence intervals for the calculated signal strengths.

electron-beam density is also nonuniform, but the large radius of the ion cloud is the dominant effect in reducing the effective density. We estimate the radius of the ion cloud to be about a factor of four larger than that of the electron beam. This effective density is higher than typical densities in X-ray AGN outflows, but in the possible range of densities for X-ray binaries outflows.

Conversely, the populations of the metastable excited states of Be-like Fe and Ne are not strongly density-dependent in the regimes studied in our experiments (see Figures 8 and 10 in Appendix B). However, they significantly depend on the population of B-like ions (Figure 7), indicating that ionization from $2s^2 2p$ to $2s 2p$ configurations can play an important role in setting the metastable state populations.
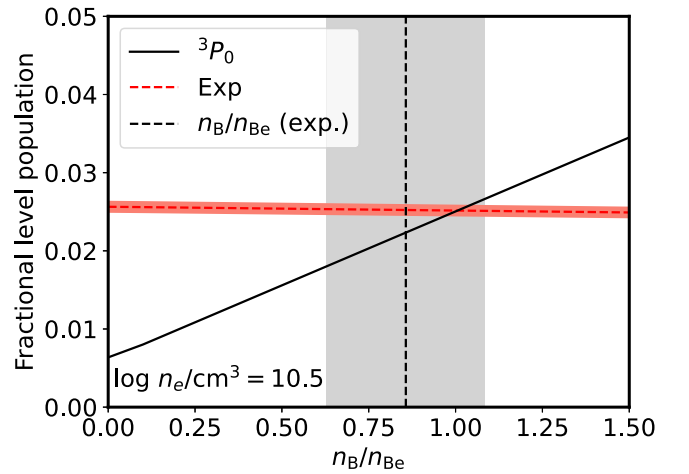


**Figure 7.** Dependence of theoretical level population of the $2p2p\,^3P_0$ state of Be-like Fe on the relative population of B-like Fe (solid black line). We compare this with the measured population (red dashed line) and charge balance (vertical black dashed line).

## 4. Conclusion

We identified photoabsorption features from metastable electronic states in three highly charged ions that are common in astrophysical plasmas, and accurately determined their excitation energies and line widths using monochromatic X-rays at high resolution. They are sufficiently separated from the ground-state transitions, so that ATHENA and partly XRISM will be able to resolve them. We also performed corresponding large-scale calculations using relativistic many-body perturbation theory with the FAC package. Using these values, we could determine the population of metastable states in our ion trap even for fractions below 1%. The obtained level populations reflect the condition of excitation by a monoenergetic electron impact, which our theoretical model satisfactorily reproduces. These results stringently benchmark large-scale electronic structure calculations needed for future space-borne X-ray missions, and can help improve our understanding of photoionized plasmas in and around, for instance, AGN and X-ray binary systems. Future measurements will add simultaneous measurement of photoions (Steinbrügge et al. 2015), enabling extraction of radiative and Auger–Meitner branching ratios and yielding accurate cross sections for the key processes governing the ionization balance of astrophysical and laboratory plasmas.

## Appendix A
## Polarization Effects

Both beamlines where we performed the reported experiments deliver highly polarized photon beams (Circular at P04 and linear at P01). This leads to polarized excited states and nonuniform angular distributions of the emitted photons during the decay of these states. These distributions can be described by

$$W(\theta) \propto 1 + \frac{\beta}{2}(3\cos^2\theta - 1) \quad \text{linear pol.} \tag{A1}$$

$$W(\theta) \propto 1 - \frac{\beta}{4}(3\cos^2\theta - 1) \quad \text{circular pol.} \tag{A2}$$

The anisotropy coefficient $\beta$ depends on the angular momenta $J_i$, $J_e$, $J_f$ of the initial, excited, and final states

$$\beta = 3(-1)^{1+J_i-J_f}(2J_e+1)$$
$$\times \begin{Bmatrix} 1 & 1 & 2 \\ J_e & J_e & J_f \end{Bmatrix}\begin{Bmatrix} 1 & 1 & 2 \\ J_e & J_e & J_i \end{Bmatrix}, \tag{A3}$$

where $\{\cdots\}$ are the 6-$j$ Wigner symbols. In the present setup, the detector was mounted at $\theta = 90°$, so the effect of the polarization can be reduced to a factor of

$$W(\theta) \propto P = 1 - \beta(J_i, J_e, J_f)/2 \quad \text{linear pol.} \tag{A4}$$

$$W(\theta) \propto P = 1 + \beta(J_i, J_e, J_f)/4 \quad \text{circular pol.} \tag{A5}$$

To reproduce the measured spectra, the calculated line strength $S$ has to be multiplied by this factor. As the excited states could decay to different final states, this factor has to be applied for each channel separately. Thus, the effective factor for a line is
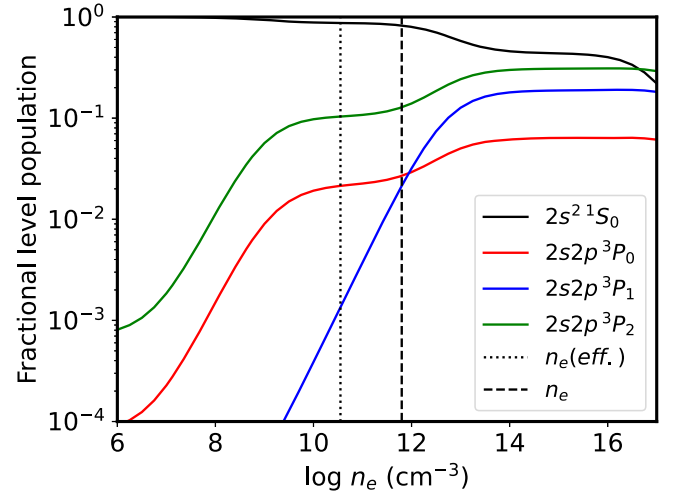
$$P_{eff} = \frac{\sum_f S_f * P(J_i, J_e, J_f)}{\sum_f S_f} \tag{A6}$$

where the sum goes over all possible final states $f$.

## Appendix B
## Plots of Dependence of Metastable Level Populations on Density and Charge Balance

In Figures 8–12 in this appendix we show additional results obtained by the FAC collisional radiative model described in the main text.
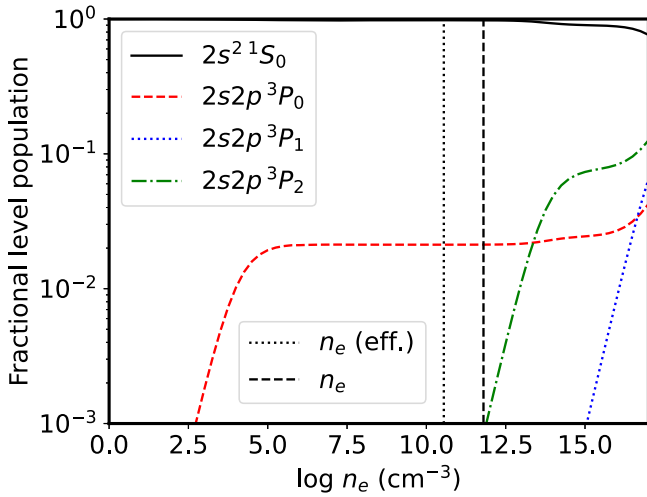
### B.1. Be-like Ne VII



**Figure 8.** Fractional populations of metastable states of Be-like Ne evaluated as a function of the electron density at an electron-beam energy close to that of our experiment ($E = 360$ eV). The population of B-like Ne is set to be 40% of the Be-like one. The calculated electron density inside the beam (black dashed line) and the estimated effective electron density seen by the ions (black dotted line) are shown. In these regimes, the dependence of the population of $2s2p\,^3P_2$ on density is weak.
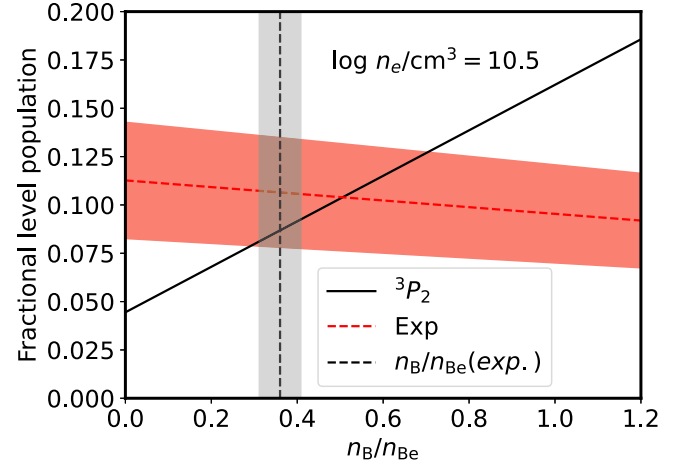


**Figure 9.** Dependence of the theoretical level population of $2p2p\,^3P_2$ state of Be-like Ne on the relative population of B-like Ne (solid black line). We compare this with the measured population (horizontal red dashed line) and charge balance (vertical black dashed line).

### B.2. Be-like Fe XXIII



**Figure 10.** Density dependence of the theoretical level populations for metastable states of Be-like Fe. The estimated electron density (black dashed line) and effective electron density (black dotted line) are shown. In the density regime of our experiment, the population of the $2s2p\,^3P_0$ state is insensitive to the electron density.

### B.3. C-like Fe XXI
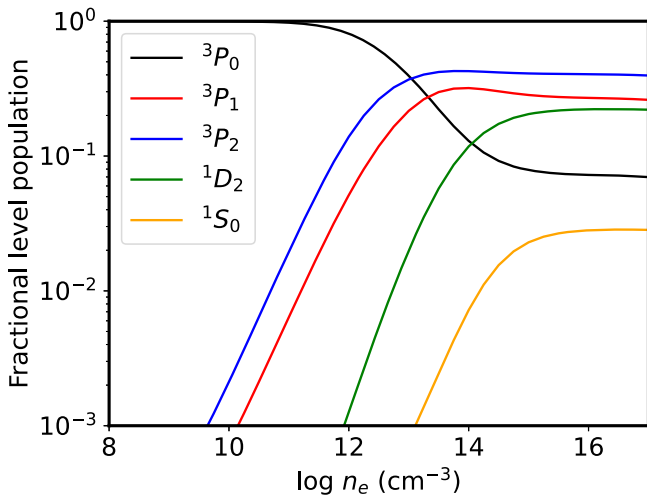


**Figure 11.** Fractional populations of metastable states of C-like Fe evaluated as a function of the electron density at an electron energy close to that of our experiment ($E = 2000$ eV). The N-like and C-like fractions are set to be equal.
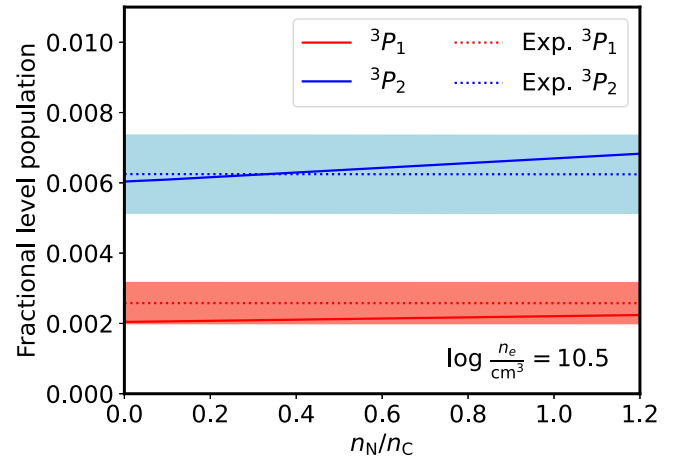


**Figure 12.** Fractional populations of metastable states of C-like Fe evaluated as a function of the relative abundance of N-like Fe at conditions close to those of our experiment ($E = 2000$ eV, $\log n_e = 10.5$). The metastable level populations weakly increase together with the relative fraction of N-like Fe. There is no dependence on the B-like Fe abundance (not shown).

## ORCID iDs

René Steinbrügge ⓘ https://orcid.org/0000-0001-7442-1260
Steffen Kühn ⓘ https://orcid.org/0000-0003-0943-2101
Fabrizio Nicastro ⓘ https://orcid.org/0000-0002-6896-1364
Ming Feng Gu ⓘ https://orcid.org/0000-0001-9136-8449
Moto Togawa ⓘ https://orcid.org/0000-0003-4571-2282
Moritz Hoesch ⓘ https://orcid.org/0000-0002-0114-2110
Florian Trinter ⓘ https://orcid.org/0000-0002-0891-9180
Sonja Bernitt ⓘ https://orcid.org/0000-0002-1976-5121
Chintan Shah ⓘ https://orcid.org/0000-0002-6484-3803
Maurice A. Leutenegger ⓘ https://orcid.org/0000-0002-3331-7595
José R. Crespo López-Urrutia ⓘ https://orcid.org/0000-0002-2937-8037

## References

Al Shorman, M. M., Gharaibeh, M. F., Bizau, J. M., et al. 2013, JPhB, 46, 195701
Asplund, M., Grevesse, N., Sauval, A. J., & Scott, P. 2009, ARA&A, 47, 481
Bahrdt, J., Baecker, H., Frentrup, W., et al. 2008, Proc. of EPAC08 (European Physical Society Accelerator Group), WEPC096, https://accelconf.web.cern.ch/e08/papers/wepc096.pdf
Barret, D., Decourchelle, A., Fabian, A., et al. 2020, AN, 341, 224
Barret, D., Lam Trong, T., den Herder, J.-W., et al. 2016, Proc. SPIE, 9905, 99052F
Beiersdorfer, P., Schweikhard, L., Crespo López-Urrutia, J. R., & Widmann, K. 1996, RScI, 67, 3818
Bizau, J. M., Cubaynes, D., Guilbaud, S., et al. 2015, PhRvA, 92, 023401
Bockasten, K., Hallin, R., & Hughes, T. 1963, PPS, 81, 522
Cen, R., & Ostriker, J. P. 2006, ApJ, 650, 560
Gu, M. F. 2008, CaJPh, 86, 675
Gu, M. F., Holczer, T., Behar, E., & Kahn, S. M. 2006, ApJ, 641, 1227

Kaastra, J., Mewe, R., Liedahl, D., Komossa, S., & Brinkman, A. 2000, A&A, 354, L83

Kaspi, S., Brandt, W. N., Netzer, H., et al. 2000, ApJ, 535, L17

Kramida, A., & Buchet-Poulizac, M.-C. 2006, EPJD, 38, 265

Krolik, J. H., & Kriss, G. A. 1995, ApJ, 447, 512

Kühn, S., Shah, C., Crespo López-Urrutia, J. R., et al. 2020, PhRvL, 124, 225001

Laha, S., Reynolds, C. S., Reeves, J., et al. 2021, NatAs, 5, 13

Leutenegger, M., Kühn, S., Micke, P., et al. 2020, PhRvL, 125, 243001

Levine, M., Marrs, R., Henderson, J., Knapp, D., & Schneider, M. B. 1988, PhST, 22, 157

Levine, M. A., Marrs, R. E., Bardsley, J. N., et al. 1989, NIMPB, 43, 431

Mao, J., Kaastra, J., Mehdipour, M., et al. 2017, A&A, 607, A100

McKernan, B., Yaqoob, T., & Reynolds, C. S. 2007, MNRAS, 379, 1359

McLaughlin, B. M., Bizau, J.-M., Cubaynes, D., et al. 2016, MNRAS, 465, 4690

Micke, P., Kühn, S., Buchauer, L., et al. 2018, RScI, 89, 063109

Miller, J. M., Raymond, J., Reynolds, C. S., et al. 2008, ApJ, 680, 1359

Müller, A., Bernhardt, D., Borovik, A., et al. 2017, ApJ, 836, 166

Müller, A., Schippers, S., Phaneuf, R. A., et al. 2014, JPhB, 47, 135201

Nandra, K., & Pounds, K. A. 1992, Natur, 359, 215

Nicastro, F., Fiore, F., Perola, G. C., & Elvis, M. 1999, ApJ, 512, 184

Paerels, F., Cottam, J., Sako, M., et al. 2000, ApJ, 533, L135

Palmeri, P., Mendoza, C., Kallman, T. R., & Bautista, M. A. 2003, A&A, 403, 1175

Penetrante, B. M., Bardsley, J. N., Levine, M. A., Knapp, D. A., & Marrs, R. E. 1991, PhRv, 43, 4873

Rudolph, J. K., Bernitt, S., Epp, S. W., et al. 2013, PhRvL, 111, 103002

Scully, S. W. J., Aguilar, A., Emmons, E. D., et al. 2005, JPhB, 38, 1967

Shabaev, V. M., Tupitsyn, I. I., & Yerokhin, V. A. 2015, CoPhC, 189, 175

Simon, M. C., Crespo López-Urrutia, J. R., Beilmann, C., et al. 2010b, PhRvL, 105, 183001

Simon, M. C., Schwarz, M., Epp, S. W., et al. 2010a, JPhB, 43, 065003

Steinbrügge, R., Bernitt, S., Epp, S. W., et al. 2015, PhRvA, 91, 032502

Tashiro, M., Maejima, H., Toda, K., et al. 2018, Proc. SPIE, 10699, 1069922

Tombesi, F., Cappi, M., Reeves, J. N., et al. 2013, MNRAS, 430, 1102

Viefhaus, J., Scholz, F., Deinert, S., et al. 2013, NIMPA, 710, 151

Wargelin, B. J., Kahn, S. M., & Beiersdorfer, P. 2001, PhRvA, 63, 022710

Wille, H.-C., Franz, H., Röhlsberger, R., Caliebe, W. A., & Dill, F.-U. 2010, JPhCS, 217, 012008

XRISM Science Team 2020, arXiv:2003.04962

Yerokhin, V. A., & Surzhykov, A. 2019, JPCRD, 48, 033104